

FrePolad: Frequency-Rectified Point Latent Diffusion for Point Cloud Generation

Chenliang Zhou Fangcheng Zhong Param Hanji Zhilin Guo Kyle Fogarty
 Alejandro Sztrajman Hongyun Gao
 Cengiz Oztireli

Department of Computer Science and Technology, University of Cambridge

chenliang.zhou@cst.cam.ac.uk

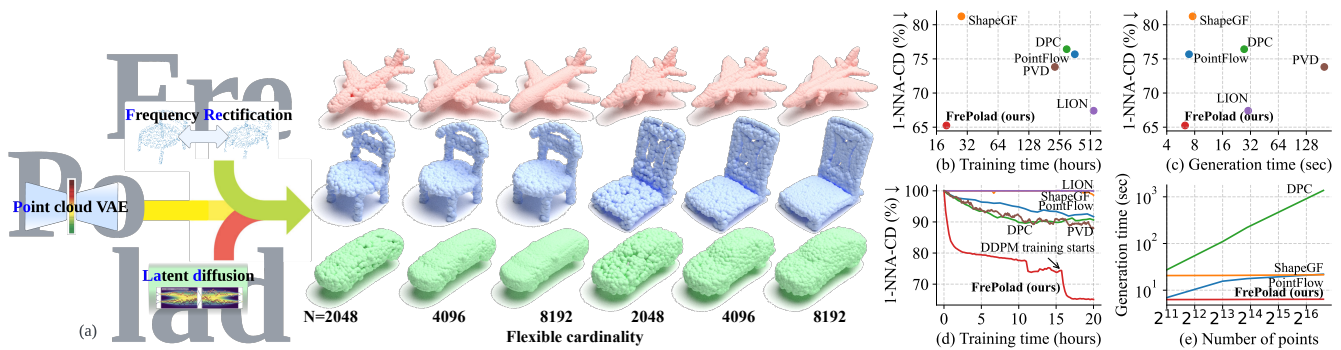


Figure 1. (a) FrePolad combines novel frequency rectification with a point cloud VAE and a DDPM-based prior to generate point clouds with superior quality, diversity, and flexibility in cardinality. Plots show on the right (b) training and (c) generation costs vs. final validation score measured by 1-NNA-CD (\downarrow), (d) learning curves for the first 20 hours of training, and (e) generation cost for synthesizing different numbers of points

Abstract

We propose FrePolad: frequency-rectified point latent diffusion, a point cloud generation pipeline integrating a variational autoencoder (VAE) with a denoising diffusion probabilistic model (DDPM) for the latent distribution. FrePolad simultaneously achieves high quality, diversity, and flexibility in point cloud cardinality for generation tasks while maintaining high computational efficiency. The improvement in generation quality and diversity is achieved through (1) a novel frequency rectification module via spherical harmonics designed to retain high-frequency content while learning the point cloud distribution; and (2) a latent DDPM to learn the regularized yet complex latent distribution. In addition, FrePolad supports variable point cloud cardinality by formulating the sampling of points as conditional distributions over a latent shape distribution. Finally, the low-dimensional latent space encoded by the VAE contributes to FrePolad’s fast and scalable sampling. Our quantitative and qualitative results demonstrate the state-of-the-art performance of Fre-

Polad in terms of quality, diversity, and computational efficiency.

1. Introduction

Point clouds are a widely-used 3D representation with extensive applications in 3D content creation and reconstruction [19, 21, 26, 38, 38, 45, 93, 97, 102]. Automated 3D content creation using point clouds has been extensively explored in recent studies through the adoption of generative methods, such as autoencoders [37, 96], adversarial training [38, 98], flow-based models [36, 43], and denoising diffusion probabilistic models (DDPM) [56, 88]. However, addressing the intricate task of learning the distributions of point clouds while simultaneously attaining exceptional sample quality, diversity, and computational efficiency poses a substantial challenge. For example, variational autoencoders (VAEs) [42] and generative adversarial networks (GANs) [24] tend to produce noisy or blurry outcomes [15, 18, 34], possibly attributed to the loss of high-

frequency information [15, 18, 46] caused by the *spectral bias* [39, 57] (also see Sec. 2). Excessive emphasis on generation fidelity, such as through the deployment of excessively deep networks, can lead to reduced diversity and even mode collapse [51, 99]. VAEs also struggle with the *prior hole problem* [78, 86, 87] when employing oversimplified Gaussian priors [9]. While normalizing flows [74] and DDPMs [29, 82] have emerged as powerful generative models, they face challenges in learning high-dimensional distributions, particularly for point clouds. A key issue with both classes of models is the necessity for the latent distribution to match the dimensionality of the target. Thus, despite their exceptional sample quality and diversity in various domains [13, 41, 60, 65, 83, 92], directly applying these models to point cloud generation results in only moderate success [56, 95, 102].

Generating point clouds with flexible cardinality (varying number of points) is also a critical, yet often overlooked feature in recent works. Prior works with fixed cardinalities [1, 21] often fail to incorporate the inherent property of permutation invariance in point clouds. These methods that are trained with heuristic loss functions such as Chamfer distance (CD) or earth mover’s distance (EMD) can also distort the probabilistic interpretation of VAEs [95]. Furthermore, the flexibility in cardinality is crucial for tasks involving non-uniform datasets, such as those from LIDAR scans [23, 79]. Networks with unrestricted cardinality readily scale for tasks with unspecified output point count requirements, avoiding the significant computational overhead associated with retraining fixed-cardinality models, while demonstrating superior quality compared to post-processing the point cloud with upsampling (see Sec. 5.4).

To simultaneously address the outlined challenges, we propose a novel generative framework, *FrePolad: frequency-rectified point latent diffusion*. FrePolad integrates a point cloud VAE with a latent DDPM modeling its latent distribution. Given that VAEs typically have access to a low-dimensional latent space, leveraging DDPMs to learn the VAE-encoded latent distributions enhances complex distribution modeling [63, 88], preserves high-frequency contents [76, 87], and reduces computational demands (see Sec. 5.3). Furthermore, harnessing insights from spherical harmonic analysis, we introduce a novel *frequency rectification* technique for training the point cloud VAE to further strengthen the preservation of high-frequency contents, thereby significantly boosting the sample fidelity and diversity (see Sec. 5.3). Finally, FrePolad supports a variable number of points in the training set via a permutation-invariant set encoder [67, 68]. By formulating the sampling of points as a conditional distribution over a latent shape distribution, *i.e.*, a *distribution of distributions*, FrePolad enables arbitrary cardinality in point cloud generation. Our extensive evaluation of FrePolad on the ShapeNet

dataset [6] demonstrates its state-of-the-art performance in terms of generation quality and diversity, while incurring the least computational expense (see Fig. 1).

Our contributions are summarized as follows:

- A novel point cloud generative network realized through a variational autoencoder (VAE) with a prior distribution based on a denoising diffusion probabilistic model (DDPM) (Sec. 4);
- An novel *frequency rectification* technique designed to promote the preservation of high-frequency details during VAE training (Secs. 4.1 and 4.2);
- A comprehensive demonstration of FrePolad’s state-of-the-art performance in terms of quality, diversity, and computational efficiency through extensive experiments and analysis (Sec. 5).

2. Related works

Denoising diffusion probabilistic models Recent advancements in denoising diffusion probabilistic models (DDPMs) [29, 82] have demonstrated remarkable performance in various domains, including image synthesis [3, 13, 29, 72, 76], density estimation [40], and speech synthesis [7, 32, 53]. Nonetheless, DDPMs are known to lack a low-dimensional, interpretable space [63] and to be time-inefficient during generation. Given that variational autoencoders (VAEs) typically have access to a low-dimensional latent space, researchers have explored the potential of DDPMs to model VAE-encoded latent distributions across various modalities, including images [72, 81], music [58], videos [2, 27, 101], and point cloud generation [88, 95]. Along this direction, our work further probes the efficacy of this paired framework in the domain of point cloud generation.

Point cloud generation A multitude of studies have delved into point cloud generation within various generative frameworks, including auto-regressive autoencoding [21, 37, 42, 75, 96], adversarial generation [1, 24, 38, 47, 54, 80, 98], flow-based models [14, 36, 41, 43, 95], and, recently, DDPMs [54, 56, 59, 62, 88, 93, 93, 102]. Recently, LION [88] proposes the VAE framework based on PVCNNs [54] with a hierarchical latent space modeled by two DDPMs. Nevertheless, while a hierarchical latent space can be effective in capturing complex distributions [30, 66, 72], an overly intricate network topology and multilayered latent codes – where a single layer exceeds the original point cloud’s dimensionality – may lead to challenges such as overfitting [64], lack of interpretability [100], and excessive computational cost during both training and sampling.

On the other hand, most works in point cloud generation primarily target at modeling the data distribution of point clouds within $\mathbb{R}^{3 \times N}$ with a fixed number N of points [1, 21]. The limitation of such approach has been

discussed in Sec. 1 and in many other works [56, 95]. In contrast, contemporary research has explored a different approach conceptualizing point clouds as probabilistic distributions in \mathbb{R}^3 , leading to the modeling of a *distribution of distributions* [4, 43, 56, 84, 95, 96].

Frequency analysis in VAE Variational autoencoders (VAEs) [42] are probabilistic generative networks modeling the probability distributions of datasets. A pervasive challenge associated with VAEs is their tendency to attenuate high-frequency data [17], often resulting in blurry or low-resolution samples [15, 18, 31, 34, 46]. This degradation becomes even more pronounced at higher compression rates [52]. Such loss of high-frequency details can be attributed to the intrinsic *spectral bias* in general neural network layers [39, 57, 70, 85] and/or to the upsampling modules in VAEs [5, 16, 91] during reconstruction or generation.

Various VAE architectures have been proposed to promote data reconstruction in the frequency domain [22, 33, 94]. Predominantly, these architectures utilize Fourier features [71] or positional encoding [57, 89] to preserve high-frequency details [12, 22, 33, 52]. Yet, a limitation exists: they lack generalizability to point cloud data since Fourier analysis requires data with a well-defined grid structure – such as 2D grids in images or 3D grids in voxels. Drawing inspiration from [61], in Secs. 4.1 and 4.2, we adopt spherical harmonic analysis for frequency information extraction from point clouds.

3. Background

3.1. Variational Autoencoder

We use a variational autoencoder (VAE) [42] as our latent distribution model as it provides access to a low-dimensional latent space and has been successfully applied to generate point clouds [49, 50, 90]. VAEs are probabilistic generative models that can model a probability distribution of a given dataset \mathcal{X} . A VAE consists of an encoder $q_\psi(\mathbf{z}|\mathbf{X})$ and a decoder $p_\xi(\mathbf{X}|\mathbf{z})$ parametrized by ψ and ξ , respectively. Assuming that the latent codes $\mathbf{z} \in \mathbb{R}^{D_z}$ follow a prior distribution $p(\mathbf{z})$, the encoder and decoder are jointly trained to maximize the *evidence lowerbound (ELBO)*:

$$\mathcal{L}_{\text{ELBO}}(\psi, \xi; \mathbf{X}) := \mathbb{E}_{q_\psi(\mathbf{z}|\mathbf{X})} [\log p_\xi(\mathbf{X}|\mathbf{z})] - \mathcal{D}_{\text{KL}}(q_\psi(\mathbf{z}|\mathbf{X}), p(\mathbf{z})), \quad (1)$$

where $\mathcal{D}_{\text{KL}}(\cdot, \cdot)$ is the Kullback-Leibler divergence between the two distributions [11].

3.2. Denoising Diffusion Probabilistic Model

Our generative framework leverages a denoising diffusion probabilistic model (DDPM) [29, 82] to model the complexity of the VAE latent space. Given a data sample

$\mathbf{z} \sim p(\mathbf{z})$, at each time step $t = 1, 2, \dots, T$, DDPMs gradually transform $\mathbf{z} = \mathbf{z}_0$ into \mathbf{z}_T by adding noise in a Markovian diffusion process according to a predetermined variance schedule $\{\beta_t\}_t$. If T is sufficiently large (1000 steps in practice), $p(\mathbf{z}_T)$ will approach the standard Gaussian distribution $\mathcal{N}(0, I)$. Furthermore, since all transition kernels of the diffusion process are Gaussian: $p(\mathbf{z}_t|\mathbf{z}_{t-1}) \sim \mathcal{N}(\mathbf{z}_t; \sqrt{1 - \beta_t}\mathbf{z}_{t-1}, \beta_t I), \forall t$, samples from the intermediate distributions can be directly generated in a single step:

$$\mathbf{z}_t = \alpha_t \mathbf{z}_0 + \gamma_t \epsilon, \quad (2)$$

where $\alpha_t := \prod_{i=1}^t \sqrt{1 - \beta_i}$, $\gamma_t := \sqrt{1 - \alpha_t^2}$, and $\epsilon \sim \mathcal{N}(0, I)$. The objective is to train a parametric model $\epsilon_\zeta(\mathbf{z}_t, t)$ by minimizing the simplified denoising score matching objective,

$$\mathcal{L}_{\text{DDPM}}(\zeta) := \mathbb{E}_{p(\mathbf{z}_0), t \sim \mathcal{U}(1, T), \epsilon \sim \mathcal{N}(0, I)} [\|\epsilon - \epsilon_\zeta(\mathbf{z}_t, t)\|_2^2], \quad (3)$$

where $\mathcal{U}(1, T)$ is the uniform distribution on $\{1, 2, \dots, T\}$.

During inference, the network allows sampling through an iterative procedure since the learned distribution can be factorized as

$$p_\zeta(\mathbf{z}) = p(\mathbf{z}_T) p_\zeta(\mathbf{z}|\mathbf{z}_T) = p(\mathbf{z}_T) \prod_{t=1}^T p_\zeta(\mathbf{z}_{t-1}|\mathbf{z}_t) \quad (4)$$

for $p(\mathbf{z}_T) := \mathcal{N}(0, I)$.

For a more detailed derivation, please refer to Sec. A in the supplementry.

3.3. Spherical Harmonics

The spherical harmonics [10] are a set of base functions $Y_{l,m} : S^2 \rightarrow \mathbb{C}$ defined on a unit sphere S^2 indexed by the degree $l \geq 0$ and the order m ($-l \leq m \leq l$). They form an orthonormal basis for square-integrable functions defined on the unit sphere $L^2(S^2)$ [70]; *i.e.*, every such function f can be represented as a series of $Y_{l,m}$ by

$$f(\theta, \varphi) = \sum_{l=0}^{\infty} \sum_{m=-l}^l c_{l,m} Y_{l,m}(\theta, \varphi). \quad (5)$$

where the coefficients $c_{l,m}$ can be calculated by

$$c_{l,m} = \int_0^{2\pi} \int_0^\pi f(\theta, \varphi) \overline{Y_{l,m}}(\theta, \varphi) \sin(\theta) d\theta d\varphi. \quad (6)$$

Similar to Fourier analysis [20], spherical harmonics cast spatial data into the spectral domain, allowing the extraction of frequency-specific information: coefficients $c_{l,m}$ with a higher degree measure the intensity of the original data in a higher-frequency domain. Please refer to Sec. B in the supplementary for more details about spherical harmonics.

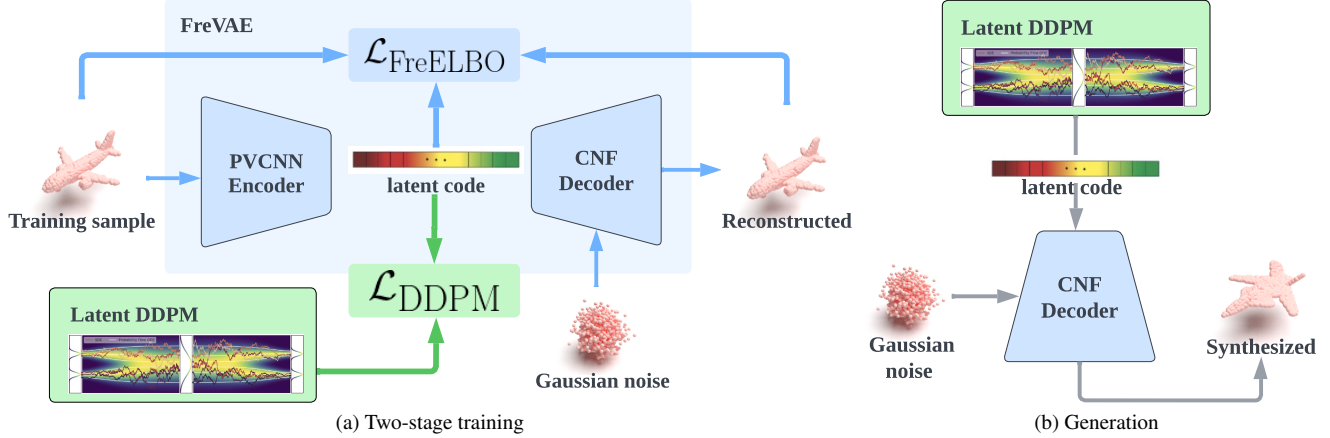


Figure 2. FrePolad is architected as a point cloud VAE, with an embedded latent DDPM to represent the latent distribution. (a) Two-stage training: in the first stage (blue), the VAE is optimized to maximize the FreELBO Eq. (15) with a standard Gaussian prior; in the second stage (green), while fixing the VAE, the latent DDPM is trained to model the latent distribution. (b) Generation: conditioned on a shape latent sampled from the DDPM, the CNF decoder transforms a Gaussian noise input into a synthesized shape.

4. Formulation

We aim to learn a generative model to synthesize point clouds $\mathbf{X} \in \mathbb{R}^{3 \times N_{\mathbf{x}}}$ consisting of $N_{\mathbf{x}}$ points with a distribution $p(\mathbf{X})$. Following [95], we treat each \mathbf{X} as a distribution $p(\mathbf{x}|\mathbf{z})$ over its points $\mathbf{x} \in \mathbb{R}^3$, conditioned on the latent vector $\mathbf{z} \sim p(\mathbf{z})$ of the underlying shape. Note that once $p(\mathbf{x}|\mathbf{z})$ is properly learned, the cardinality of the point cloud is unrestricted as one can sample an arbitrary number of points from this distribution.

Figure 2 presents an overview of our generative model, *frequency-rectified point latent diffusion (FrePolad)*. FrePolad amalgamates a point cloud VAE that models $p(\mathbf{x}|\mathbf{z})$ with a DDPM modeling its latent distribution $p(\mathbf{z})$. Synthesis is performed by sampling a shape latent from the DDPM which is subsequently decoded into a point cloud. To train the VAE, we leverage spherical harmonics and extract frequency information from point clouds (Sec. 4.1). Then, we formulate a novel frequency rectification module that encourages the reconstruction of high-frequency regions (Sec. 4.2). In addition, we employ a latent DDPM for enhanced expressiveness, continuous preservation of high-frequency contents, and reduced dimensionality. Collectively, we harmonize these components for our model, FrePolad, to facilitate point cloud generation (Sec. 4.4).

4.1. Frequency Extraction via Spherical Harmonics

In order to extract frequency information with spherical harmonics (Eq. (5)), we seek to represent the underlying surface of a point cloud $\mathbf{X} \in \mathbb{R}^{3 \times N_{\mathbf{x}}}$ consisting of $N_{\mathbf{x}}$ points by a continuous function on the unit sphere, *i.e.*, $f_{\mathbf{X}}(\theta, \varphi)$. Note that, with this representation, we assume the surface is a *star domain*. We start by expressing each 3D point in spherical coordinates $\mathbf{x}_i = (r_i, \theta_i, \varphi_i)$. Next, we construct

$f_{\mathbf{X}}$ by anchoring each point $\mathbf{x}_i \in \mathbf{X}$ to its radius r_i and interpolating in the rest of the domain:

$$f_{\mathbf{X}}(\theta, \varphi) := \begin{cases} r & (\theta, \varphi, r) \in \mathbf{X} \\ \sum_{\substack{(\theta_i, \varphi_i) \\ \in \mathcal{H}_{\mathbf{X}}(\theta, \varphi)}} w_i(\theta, \varphi) r_i & \text{otherwise} \end{cases}, \quad (7)$$

where $\mathcal{H}_{\mathbf{X}}(\theta, \varphi)$ is the set of k closest neighbors (θ_i, φ_i) of (θ, φ) with $(r_i, \theta_i, \varphi_i) \in \mathbf{X}$ for some r_i , determined according to the following distance function d ,

$$d_{\text{sphere}}((\theta, \varphi), (\theta', \varphi')) := \sqrt{2 - 2[\sin \theta \sin \theta' \cos(\varphi - \varphi') + \cos \theta \cos \theta']}, \quad (8)$$

and $w_i(\theta, \varphi)$ are the weights.

Since closer points should have larger weights, $\{w_i(\theta, \varphi)\}_i$ should be a decreasing sequence on $d_{\text{sphere}}((\theta, \varphi), (\theta_i, \varphi_i))$. A suitable candidate is the normalized Gaussian function with standard deviation σ_{KNN} :

$$w'_i(\theta, \varphi) := e^{-\frac{d_{\text{sphere}}^2((\theta, \varphi), (\theta_i, \varphi_i))}{2\sigma_{\text{KNN}}^2}} \quad \text{and} \quad w_{ij} := \frac{w'_i}{\sum_j w'_j}. \quad (9)$$

Defining $f_{\mathbf{X}}$ in this way presents limitations for point clouds with non-star-domain shapes. Specifically, at some values of θ and ϕ , there may exist multiple points from semantically different regions of the point cloud. Nevertheless, we found this formulation to be computationally efficient and empirically superior to more complex alternatives (see the ablation study in Sec. 5.3 for more details).

After representing \mathbf{X} by $f_{\mathbf{X}}$, we can extract frequency information by computing its spherical harmonic coefficients

$c_{l,m}^{\mathbf{X}}$ via Eq. (6); these coefficients reveal the original point cloud \mathbf{X} in frequency domains. We show an example of a point cloud and its representative function in spherical as well as frequency domains in Fig. 3 (first row).

4.2. Frequency-Rectified VAE

As discussed earlier, VAEs suffer from losing high-frequency data, and existing remedies do not generalize well to point clouds [15, 18, 31, 34, 46]. To mitigate this problem, we utilize the frequency information extracted in Sec. 4.1 and propose *frequency rectification* in training the VAE that promotes the preservation of high-frequency information.

We first define a frequency-rectified distance $d_{\text{Fre}}(\mathbf{X}, \mathbf{X}')$ between two point clouds \mathbf{X} and \mathbf{X}' :

$$d_{\text{Fre}}(\mathbf{X}, \mathbf{X}') := \sum_{l=0}^{\infty} \sum_{m=-l}^l r_l \left\| c_{l,m}^{\mathbf{X}} - c_{l,m}^{\mathbf{X}'} \right\|_2^2, \quad (10)$$

where $\{r_l\}_l$ is a sequence of increasing *frequency rectifiers* that weight higher-degree spherical harmonic coefficients more. In practice, we restrict the infinite sum and evaluate the first $L + 1$ terms. The frequency rectifiers are given by the Gaussian function:

$$r_l := e^{-\frac{(L-l)^2}{2\sigma_{\text{Fre}}^2}}. \quad (11)$$

A frequency rectified loss between encoder and decoder distributions can be obtained by taking the expectation over point clouds \mathbf{X}' learned by the VAE:

$$\mathcal{L}_{\text{Fre}}(\psi, \xi; \mathbf{X}) := \mathbb{E}_{\mathbf{z} \sim q_{\psi}(\mathbf{z}|\mathbf{X}), \mathbf{X}' \sim p_{\xi}(\mathbf{X}|\mathbf{z})} [d_{\text{Fre}}(\mathbf{X}, \mathbf{X}')] \quad (12)$$

In order to encourage the reconstruction of high-frequency regions, we introduce a constraint while maximizing the ELBO (Eq. (1)):

$$\begin{aligned} \max_{\psi, \xi} \mathbb{E}_{\mathbf{X} \sim p(\mathbf{X})} [\mathcal{L}_{\text{ELBO}}(\psi, \xi; \mathbf{X})] \\ \text{s.t. } \mathbb{E}_{\mathbf{X} \sim p(\mathbf{X})} [\mathcal{L}_{\text{Fre}}(\psi, \xi; \mathbf{X})] < \delta, \end{aligned} \quad (13)$$

where $\delta > 0$ controls the strength of this constraint. Leveraging Karush–Kuhn–Tucker (KKT) methods [35, 44], we can re-write the above constrained optimization problem (13) as a Lagrange function whose optimal point is a global maximum over the domain of (ψ, ξ) :

$$\mathcal{F}(\psi, \xi, \eta; \mathbf{X}) := \mathcal{L}_{\text{ELBO}}(\psi, \xi; \mathbf{X}) - \eta (\mathcal{L}_{\text{Fre}}(\psi, \xi; \mathbf{X}) - \delta), \quad (14)$$

where η is the KKT multiplier. Since $\delta > 0$, we now have a lower-bound on the ELBO:

$$\begin{aligned} \mathcal{F}(\psi, \xi, \eta; \mathbf{X}) &\geq \mathcal{L}_{\text{ELBO}}(\psi, \xi; \mathbf{X}) - \eta \mathcal{L}_{\text{Fre}}(\psi, \xi; \mathbf{X}) \\ &=: \mathcal{L}_{\text{FreELBO}}(\psi, \xi, \eta; \mathbf{X}). \end{aligned} \quad (15)$$

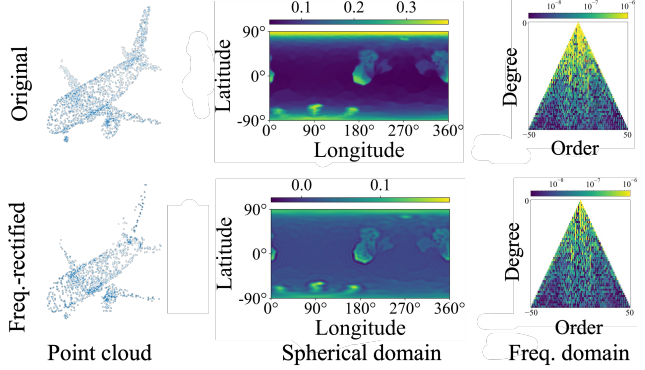


Figure 3. A point cloud before and after frequency rectification and its representative function in spherical and frequency domains. Frequency rectification shifts points to more complex, less smooth regions and increases the relative importance of higher-frequency features, where VAEs can give more attention during reconstruction. Note that the frequency rectified point cloud in the second row is only for visualization; our framework does not explicitly generate such a point cloud during training.

Our encoder and decoder networks are trained by maximizing the novel *frequency-rectified evidence lowerbound* (*FreELBO*) $\mathcal{L}_{\text{FreELBO}}$. The hyperparameter η trades-off reconstruction quality between the spatial and spectral domains. When $\eta = 0$, the training objective is the same as the original ELBO Eq. (1); when $\eta > 0$, inaccuracies in reconstructing high-frequency regions are penalized more.

An example of a frequency-rectified point cloud is shown in Fig. 3. We observe that after frequency rectification, points shift to more complex or less smooth regions in the point clouds, corresponding to higher frequency areas. Additionally, in the frequency domain, we see that as lower-frequency features (with lower degrees) are decayed by the rectifiers Eq. (11), the relative significance of higher-frequency features amplifies. Consequently, our VAE prioritizes the reconstruction in these regions.

4.3. DDPM-Based Prior

Although it is possible to sample shape latents from a simple Gaussian prior for generation, evidence suggests that such a restricted prior cannot accurately capture complex encoder distributions, $q_{\psi}(\mathbf{z}|\mathbf{X})$. This is known as the *prior hole problem* [78, 86, 87], and tends to curtail the performance of VAEs [9], resulting in the poor reconstructions in our ablation study (see Sec. 5.3). To address this, we employ a DDPM to model the VAE’s latent distribution [76]. The DDPM is trained on the latents \mathbf{z} directly sampled from $q_{\psi}(\mathbf{z}|\mathbf{X})$. Since the original prior is insufficient, the DDPM learns a more expressive distribution $p_{\zeta}(\mathbf{z})$, better matches the true latent distribution $p(\mathbf{z})$, and functions as the VAE’s prior. Combining latent DDPM with a VAE-based model helps achieve a near-ideal equilibrium between minimizing

complexity and ensuring perceptual fidelity [76, 87]. Crucially, the high-frequency details maintained by frequency rectification during encoding stage remain undisturbed. Additionally, learning the distribution of shape latents instead of point clouds significantly reduces the training and sampling cost (see Tab. 3) due to the reduced dimensionality. This enables scalable generation of much denser point clouds (see Fig. 5).

4.4. FrePolad

With all the building blocks, we present our new generative model for point cloud generation: *FrePolad: frequency-rectified point latent diffusion*. The overall structure of our framework is presented in Fig. 2.

Components The VAE encoder $q_\psi(\mathbf{z}|\mathbf{X})$ is a Point-Voxel CNN (PVCNN) [54, 102] parametrized by ψ . PVCNNs efficiently combine the point-based processing of PointNets [67, 68] with the strong spatial inductive bias of convolutions. Our encoder accommodates point clouds of variable cardinalities and is permutation-invariant.

In order to support flexible cardinality while synthesizing point clouds, we interpret each point cloud \mathbf{X} as a distribution $p(\mathbf{x}|\mathbf{z})$ of its constituent points conditioned on the shape latent \mathbf{z} . Assuming independence among the points in a point cloud, we model the decoder distribution as

$$p_\xi(\mathbf{X}|\mathbf{z}) := \prod_{\mathbf{x} \in \mathbf{X}} p_\xi(\mathbf{x}|\mathbf{z}). \quad (16)$$

The decoder is implemented using a conditional continuous normalizing flow (CNF) [8, 25, 74]. Here, a sampled point \mathbf{x} is the result of transforming some initial point $\mathbf{x}(0) \sim p(\mathbf{x}(0)) := \mathcal{N}(0, I)$, conditioned on the shape latent \mathbf{z} . The invertible nature of CNFs offers a high degree of interpretability and also allows the precise computation of data likelihood $p(\mathbf{x}|\mathbf{z})$ by moving the transformed points back to the prior distribution. For more details, please refer to Sec. C in the supplementary.

The latent DDPM $p_\zeta(\mathbf{z})$ is parametrized by ζ , realized through a U-Net backbone [77] following [76].

Training Following common practice [4, 18, 73, 76], we perform a two-stage training. In the first stage, we train the VAE network by maximizing the FreELBO Eq. (15) with the prior $p(\mathbf{z}) := \mathcal{N}(0, I)$. In the second stage, we freeze the VAE network and train the DDPM on the latent vectors sampled from the encoder $q_\psi(\mathbf{z}|\mathbf{X})$ by minimizing the objective function Eq. (3).

Generation During generation, new point clouds of arbitrary cardinality can be generated by first sampling a shape latent \mathbf{z} from the DDPM $p_\zeta(\mathbf{z})$ following Eq. (4) and then

sampling the decoder $p_\xi(\mathbf{X}|\mathbf{z})$ following Eq. (16): Formally, the generation process of FrePolad is defined by

$$p_{\xi, \zeta}(\mathbf{X}) := p_\zeta(\mathbf{z})p_\xi(\mathbf{X}|\mathbf{z}). \quad (17)$$

5. Experiments

In this section, we provide experiments demonstrating FrePolad’s performance in point cloud generation. Please refer to Sec. D in the supplementary for training and hyperparameter details.

5.1. Dataset

To benchmark FrePolad against existing methods, we employ ShapeNet [6], a widely used dataset for 3D generative task assessments. Following prior work [56, 88, 95, 102], we train on three categories: *airplane*, *chair*, and *car*. We follow the dataset splits and preprocessing established in PointFlow [95]. Unless stated otherwise, each point cloud consists of 2048 points for each shape.

5.2. Evaluation metrics

In line with previous works [56, 88, 95, 102], we employ 1-nearest neighbor (1-NNA) [55], computed using both Chamfer distance (CD) and earth mover distance (EMD). 1-NNA assesses the similarity between two 3D shape distributions, considering both diversity and quality [95]. Section E in the supplementary provides further comparisons with two other metrics: minimum matching distance (MMD) [1] and coverage (COV) [1].

5.3. Results

Point cloud generation In Tab. 1, we benchmark our model, FrePolad, against several recent works. Demonstrating high generation fidelity and diversity, our model consistently surpasses most baselines and approaches the ground truth (training set). Importantly, FrePolad attains excellent results comparable to the state-of-the-art model LION [88] despite a simpler architecture that is computationally efficient during both training and inference (see the efficiency evaluation below). Further, by modeling each point cloud as a point distribution over a shape latent, our method facilitates sampling point clouds with arbitrary cardinality – a feature rarely available in other baselines. Figure 5 illustrates the generation with different numbers of points.

Figure 4 provides qualitative comparisons, highlighting the visually appealing and diverse point clouds generated by FrePolad across three distinct classes.

Latent interpolation Fig. 6 showcases latent interpolations facilitated by FrePolad. The smooth transitions in the interpolated shapes suggest that our network successfully captures an effective latent space of the underlying shapes.

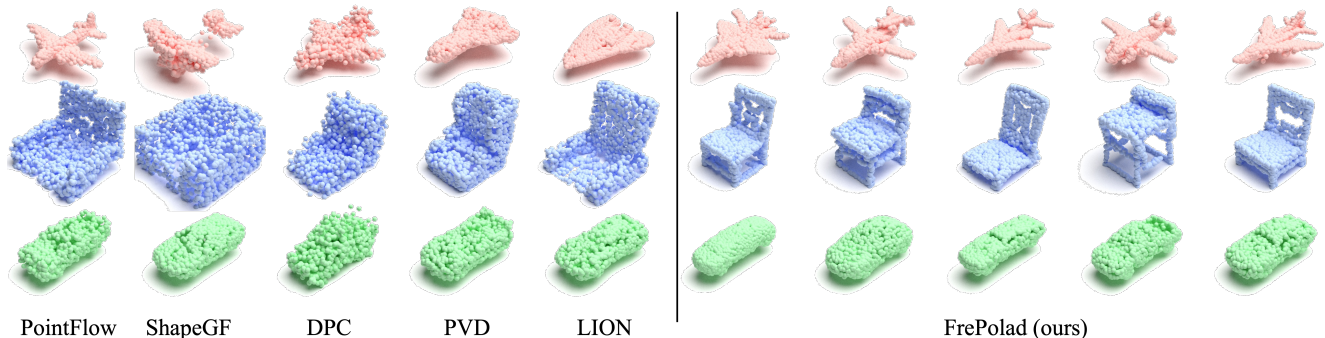


Figure 4. Generation with 2048 points for airplane, chair, and car classes. Samples generated by FrePolad have better fidelity and diversity.

Model	Airplane		Chair		Car	
	CD	EMD	CD	EMD	CD	EMD
Training set	64.44	64.07	51.28	54.76	51.70	50.00
r-GAN [1]	98.40	96.79	83.69	99.70	94.46	99.01
1-GAN/CD [1]	87.30	93.95	68.58	83.84	66.49	88.78
1-GAN/EMD [1]	89.49	76.91	71.90	64.65	71.16	66.19
PointFlow [95]	75.68	70.74	62.84	60.57	58.10	56.25
SoftFlow [36]	76.05	65.80	59.21	60.05	64.77	60.09
SetVAE [37]	76.54	67.65	58.84	60.57	59.94	59.94
ShapeGF [4]	81.23	80.86	58.01	61.25	61.79	57.24
DPF-Net [43]	75.18	65.55	62.00	58.53	62.35	54.48
DPC [56]	76.42	86.91	60.05	74.77	68.89	79.97
PVD [102]	73.82	64.81	56.26	53.32	54.55	53.83
LION [88]	67.41	61.23	53.70	52.34	53.41	51.14
FrePolad (ours)	65.25	62.10	52.35	53.23	51.89	50.26

Table 1. 1-NNA scores (\downarrow) on point cloud generation on three classes of ShapeNet dataset. FrePolad achieves significant improvement over most existing models and obtains state-of-the-art results with simpler and more flexible structure.

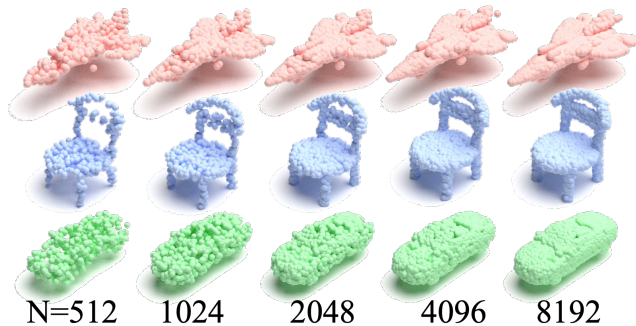


Figure 5. FrePolad supports flexibility in the cardinality of the synthesized point clouds.

Ablation study In Tab. 2 and Fig. 7 we also include quantitative and qualitative comparisons of three simplified variants of FrePolad. We selectively omit some components such as the frequency rectification and/or the latent DDPM:

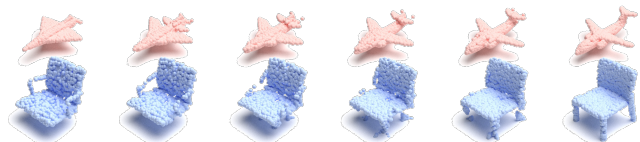


Figure 6. Interpolation of shapes in the VAE latent space.

Model	Airplane		Chair		Car	
	CD	EMD	CD	EMD	CD	EMD
Po	85.93	85.94	94.53	99.22	100.0	100.0
FrePo	80.38	80.38	89.06	82.19	89.22	84.53
Polad	69.26	65.26	57.35	61.52	58.12	56.13
FrePolad	65.25	62.10	52.35	53.23	51.89	50.26

Table 2. Ablation study: 1-NNA scores (\downarrow) of three simplified versions of FrePolad. The frequency rectification and the latent DDPM bring significant improvement to FrePolad.

- Polad (FrePolad without frequency rectification): in the first stage of training, the VAE is trained with the standard ELBO Eq. (1) in lieu of the FreELBO Eq. (15);
- FrePo (FrePolad without latent diffusion): instead of using a latent diffusion to learn the latent distribution of VAE, we assume the prior is a standard Gaussian; and
- Po (FrePolad without both).

Our results indicate that incorporating both frequency rectification and latent DDPM substantially enhances the quality and diversity of the generated point clouds.

Computational efficiency We compare the computational efficiency of different models trained on ShapeNet airplane dataset [6]. In Tab. 3 and Fig. 1 (b) to (e), we document the computational overhead incurred by different methods during training and generation. From these results, it is evident that exhibits the most favorable computational efficiency and scalability while maintaining high generation quality. The difference becomes even more evident when generating dense point clouds containing as many as 100k

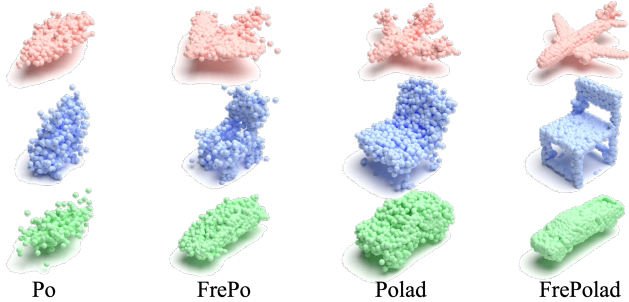


Figure 7. Ablation study: shape generation by three simplified versions of FrePolad.

Model	Train (hours)	Generation (seconds per shape)			
		2048	8192	15k	100k
PointFlow [95]	360	6.95	15.6	17.7	22.0
ShapeGF [4]	28	20.60	20.71	20.87	21.42
DPC [56]	300	27.34	110	220	1370
PVD [102]	230	200	-	-	-
LION [88]	550	30.2	-	-	-
FrePolad (ours)	20	6.30	6.32	6.35	6.41

Table 3. Computational cost of training on the airplane dataset and generation with different point cloud cardinalities. “-” means unsupported. FrePolad incurs the least computational cost and can be easily scaled up to generate significantly denser point clouds.

points.

5.4. Direct generation vs. upsampling

The flexibility of FrePolad enables the generation of arbitrarily dense point clouds. While such dense point clouds can also be acquired by upsampling sparse ones, we claim that FrePolad’s direct generation approach yields superior quality. To demonstrate this, we consider the generation of point clouds of different cardinalities containing 8192, 15k, and 100k points. We consider a few baselines that generate dense point clouds by upsampling sparser ones using recent, competitive methods. Due to the GPU memory constraints, we only sample 8192 points when evaluating 1-NNA-CD. The result is summarized in Tab. 4 (further results with other data classes or metrics can be found in Tab. 7 in the supplementary). We can observe that the direct generation by FrePolad vastly outperforms the upsampling approach in terms of generation quality and runtime. This comparison clearly highlights the advantage of FrePolad’s capability to directly generate dense point clouds.

6. Conclusion and Future Works

In this paper, we presented FrePolad, a novel method for point cloud generation. At its core, FrePolad is structured as a point cloud VAE integrated with a DDPM-based prior.

Model	1-NNA-CD (\downarrow)			Time (min)		
	8192	15k	100k	8192	15k	100k
PU-GAN [48]	100	100	100	1.17	2.44	7.55
PU-GCN [69]	100	100	100	0.83	6.67	96
Grad-PU [28]	100	100	100	0.87	2.47	68.52
FrePolad (ours)	65.31	66.87	66.25	0.11	0.11	0.11

Table 4. 1-NNA-CD (\downarrow) and time cost of the generation of dense point clouds with different cardinalities. The first three methods upsample sparse ground truths while FrePolad directly generates dense ones. FrePolad substantially outperforms all upsampling methods in terms of generation quality and runtime, demonstrating the importance of the ability to directly generate dense point clouds.

To enhance sample quality and diversity, we tailor a new frequency rectification technique that preserves the high-frequency details extracted via spherical harmonics. We also incorporate a latent DDPM to model the regularized latent space of the VAE. Additionally, to achieve flexibility in the point cloud cardinality, we perceive point clouds as distributions of their constituent points over a latent shape. Our proposed model exhibits minimal training and sampling overheads and can be easily scaled to generate highly dense point clouds. Our empirical analyses, both quantitative and qualitative, showed the state-of-the-art performance achieved by FrePolad.

We currently use the standard spherical harmonic base functions $Y_{l,m}$ in Eq. (29) on the unit sphere for frequency analysis. An interesting future direction is to investigate a more general differential analysis on manifolds where the base functions are defined on the smoothed surface derived from the original point cloud. Additionally, we aspire to explore the application of frequency rectification in other domains that deal with complex signals containing high-frequency information.

References

- [1] Panos Achlioptas, Olga Diamanti, Ioannis Mitliagkas, and Leonidas Guibas. Learning representations and generative models for 3d point clouds. In *International conference on machine learning*, pages 40–49. PMLR, 2018. 2, 6, 7, 15, 16
- [2] Andreas Blattmann, Robin Rombach, Huan Ling, Tim Dockhorn, Seung Wook Kim, Sanja Fidler, and Karsten Kreis. Align your latents: High-resolution video synthesis with latent diffusion models. In *Proceedings of the IEEE/CVF Conference on Computer Vision and Pattern Recognition*, pages 22563–22575, 2023. 2
- [3] Tim Brooks, Aleksander Holynski, and Alexei A Efros. Instructpix2pix: Learning to follow image editing instructions. In *Proceedings of the IEEE/CVF Conference on*

- Computer Vision and Pattern Recognition*, pages 18392–18402, 2023. [2](#)
- [4] Ruojin Cai, Guandao Yang, Hadar Averbuch-Elor, Zekun Hao, Serge Belongie, Noah Snavely, and Bharath Hariharan. Learning gradient fields for shape generation. In *Computer Vision—ECCV 2020: 16th European Conference, Glasgow, UK, August 23–28, 2020, Proceedings, Part III 16*, pages 364–381. Springer, 2020. [3](#), [6](#), [7](#), [8](#), [16](#)
- [5] Keshigeeyan Chandrasegaran, Ngoc-Trung Tran, and Ngai-Man Cheung. A closer look at fourier spectrum discrepancies for cnn-generated images detection. In *Proceedings of the IEEE/CVF conference on computer vision and pattern recognition*, pages 7200–7209, 2021. [3](#)
- [6] Angel X Chang, Thomas Funkhouser, Leonidas Guibas, Pat Hanrahan, Qixing Huang, Zimo Li, Silvio Savarese, Manolis Savva, Shuran Song, Hao Su, et al. Shapenet: An information-rich 3d model repository. *arXiv preprint arXiv:1512.03012*, 2015. [2](#), [6](#), [7](#)
- [7] Nanxin Chen, Yu Zhang, Heiga Zen, Ron J Weiss, Mohammad Norouzi, and William Chan. Wavegrad: Estimating gradients for waveform generation. *arXiv preprint arXiv:2009.00713*, 2020. [2](#)
- [8] Ricky TQ Chen, Yulia Rubanova, Jesse Bettencourt, and David K Duvenaud. Neural ordinary differential equations. *Advances in neural information processing systems*, 31, 2018. [6](#), [14](#)
- [9] Xi Chen, Diederik P Kingma, Tim Salimans, Yan Duan, Prafulla Dhariwal, John Schulman, Ilya Sutskever, and Pieter Abbeel. Variational lossy autoencoder. *arXiv preprint arXiv:1611.02731*, 2016. [2](#), [5](#)
- [10] Richard Courant and David Hilbert. *Methods of mathematical physics: partial differential equations*. John Wiley & Sons, 2008. [3](#), [13](#)
- [11] Imre Csiszár. I-divergence geometry of probability distributions and minimization problems. *The annals of probability*, pages 146–158, 1975. [3](#)
- [12] Steffen Czolbe, Oswin Krause, Ingemar Cox, and Christian Igel. A loss function for generative neural networks based on watson’s perceptual model. *Advances in Neural Information Processing Systems*, 33:2051–2061, 2020. [3](#)
- [13] Prafulla Dhariwal and Alexander Nichol. Diffusion models beat gans on image synthesis. *Advances in neural information processing systems*, 34:8780–8794, 2021. [2](#)
- [14] Laurent Dinh, David Krueger, and Yoshua Bengio. Nice: Non-linear independent components estimation. *arXiv preprint arXiv:1410.8516*, 2014. [2](#)
- [15] Alexey Dosovitskiy and Thomas Brox. Generating images with perceptual similarity metrics based on deep networks. *Advances in neural information processing systems*, 29, 2016. [1](#), [2](#), [3](#), [5](#)
- [16] Ricard Durall, Margret Keuper, and Janis Keuper. Watch your up-convolution: Cnn based generative deep neural networks are failing to reproduce spectral distributions. In *Proceedings of the IEEE/CVF conference on computer vision and pattern recognition*, pages 7890–7899, 2020. [3](#)
- [17] Tarik Dzanic, Karan Shah, and Freddie Witherden. Fourier spectrum discrepancies in deep network generated images. *Advances in neural information processing systems*, 33:3022–3032, 2020. [3](#)
- [18] Patrick Esser, Robin Rombach, and Bjorn Ommer. Taming transformers for high-resolution image synthesis. In *Proceedings of the IEEE/CVF conference on computer vision and pattern recognition*, pages 12873–12883, 2021. [1](#), [2](#), [3](#), [5](#), [6](#)
- [19] Haoqiang Fan, Hao Su, and Leonidas J Guibas. A point set generation network for 3d object reconstruction from a single image. In *Proceedings of the IEEE conference on computer vision and pattern recognition*, pages 605–613, 2017. [1](#)
- [20] J Fourier. Mémoire sur la propagation de la chaleur dans les corps solides (extrait). *Nouveau Bulletin des Sciences, par la Société Philomathique de Paris*, 1:112–16, 1808. [3](#), [14](#)
- [21] Matheus Gadelha, Rui Wang, and Subhransu Maji. Multiresolution tree networks for 3d point cloud processing. In *Proceedings of the European Conference on Computer Vision (ECCV)*, pages 103–118, 2018. [1](#), [2](#)
- [22] Ge Gao, Pei You, Rong Pan, Shunyuan Han, Yuanyuan Zhang, Yuchao Dai, and Hojae Lee. Neural image compression via attentional multi-scale back projection and frequency decomposition. In *Proceedings of the IEEE/CVF International Conference on Computer Vision*, pages 14677–14686, 2021. [3](#)
- [23] Andreas Geiger, Philip Lenz, Christoph Stiller, and Raquel Urtasun. Vision meets robotics: The kitti dataset. *The International Journal of Robotics Research*, 32(11):1231–1237, 2013. [2](#)
- [24] Ian Goodfellow, Jean Pouget-Abadie, Mehdi Mirza, Bing Xu, David Warde-Farley, Sherjil Ozair, Aaron Courville, and Yoshua Bengio. Generative adversarial nets. *Advances in neural information processing systems*, 27, 2014. [1](#), [2](#)
- [25] Will Grathwohl, Ricky TQ Chen, Jesse Bettencourt, Ilya Sutskever, and David Duvenaud. Ffjord: Free-form continuous dynamics for scalable reversible generative models. *arXiv preprint arXiv:1810.01367*, 2018. [6](#), [14](#)
- [26] Thibault Groueix, Matthew Fisher, Vladimir G Kim, Bryan C Russell, and Mathieu Aubry. A papier-mâché approach to learning 3d surface generation. In *Proceedings of the IEEE conference on computer vision and pattern recognition*, pages 216–224, 2018. [1](#)
- [27] Yingqing He, Tianyu Yang, Yong Zhang, Ying Shan, and Qifeng Chen. Latent video diffusion models for high-fidelity video generation with arbitrary lengths. *arXiv preprint arXiv:2211.13221*, 2022. [2](#)
- [28] Yun He, Danhang Tang, Yinda Zhang, Xiangyang Xue, and Yanwei Fu. Grad-pu: Arbitrary-scale point cloud upsampling via gradient descent with learned distance functions. In *Proceedings of the IEEE/CVF Conference on Computer Vision and Pattern Recognition*, pages 5354–5363, 2023. [8](#), [17](#)
- [29] Jonathan Ho, Ajay Jain, and Pieter Abbeel. Denoising diffusion probabilistic models. *Advances in neural information processing systems*, 33:6840–6851, 2020. [2](#), [3](#), [13](#)
- [30] Jonathan Ho, Chitwan Saharia, William Chan, David J Fleet, Mohammad Norouzi, and Tim Salimans. Cascaded

- diffusion models for high fidelity image generation. *The Journal of Machine Learning Research*, 23(1):2249–2281, 2022. [2](#)
- [31] Xianxu Hou, Linlin Shen, Ke Sun, and Guoping Qiu. Deep feature consistent variational autoencoder. In *2017 IEEE winter conference on applications of computer vision (WACV)*, pages 1133–1141. IEEE, 2017. [3](#), [5](#)
- [32] Myeonghun Jeong, Hyeongju Kim, Sung Jun Cheon, Byoung Jin Choi, and Nam Soo Kim. Diff-tts: A denoising diffusion model for text-to-speech. *arXiv preprint arXiv:2104.01409*, 2021. [2](#)
- [33] Liming Jiang, Bo Dai, Wayne Wu, and Chen Change Loy. Focal frequency loss for image reconstruction and synthesis. In *Proceedings of the IEEE/CVF International Conference on Computer Vision*, pages 13919–13929, 2021. [3](#)
- [34] Justin Johnson, Alexandre Alahi, and Li Fei-Fei. Perceptual losses for real-time style transfer and super-resolution. In *Computer Vision—ECCV 2016: 14th European Conference, Amsterdam, The Netherlands, October 11–14, 2016, Proceedings, Part II 14*, pages 694–711. Springer, 2016. [1](#), [3](#), [5](#)
- [35] William Karush. Minima of functions of several variables with inequalities as side constraints. *M. Sc. Dissertation. Dept. of Mathematics, Univ. of Chicago*, 1939. [5](#)
- [36] Hyeongju Kim, Hyeonseung Lee, Woo Hyun Kang, Joun Yeop Lee, and Nam Soo Kim. Softflow: Probabilistic framework for normalizing flow on manifolds. *Advances in Neural Information Processing Systems*, 33:16388–16397, 2020. [1](#), [2](#), [7](#), [16](#)
- [37] Jinwoo Kim, Jaehoon Yoo, Juho Lee, and Seunghoon Hong. Setvae: Learning hierarchical composition for generative modeling of set-structured data. In *Proceedings of the IEEE/CVF Conference on Computer Vision and Pattern Recognition*, pages 15059–15068, 2021. [1](#), [2](#), [7](#), [16](#)
- [38] Jaeyeon Kim, Binh-Son Hua, Thanh Nguyen, and Sai-Kit Yeung. Pointinverter: Point cloud reconstruction and editing via a generative model with shape priors. In *Proceedings of the IEEE/CVF Winter Conference on Applications of Computer Vision*, pages 592–601, 2023. [1](#), [2](#)
- [39] Soo Ye Kim, Kfir Aberman, Nori Kanazawa, Rahul Garg, Neal Wadhwa, Huiwen Chang, Nikhil Karnad, Munchurl Kim, and Orly Liba. Zoom-to-inpaint: Image inpainting with high-frequency details. In *Proceedings of the IEEE/CVF Conference on Computer Vision and Pattern Recognition*, pages 477–487, 2022. [2](#), [3](#)
- [40] Diederik Kingma, Tim Salimans, Ben Poole, and Jonathan Ho. Variational diffusion models. *Advances in neural information processing systems*, 34:21696–21707, 2021. [2](#)
- [41] Durk P Kingma and Prafulla Dhariwal. Glow: Generative flow with invertible 1x1 convolutions. *Advances in neural information processing systems*, 31, 2018. [2](#)
- [42] Diederik P Kingma and Max Welling. Auto-encoding variational bayes. *arXiv preprint arXiv:1312.6114*, 2013. [1](#), [2](#), [3](#)
- [43] Roman Klokov, Edmond Boyer, and Jakob Verbeek. Discrete point flow networks for efficient point cloud generation. In *European Conference on Computer Vision*, pages 694–710. Springer, 2020. [1](#), [2](#), [3](#), [7](#), [16](#)
- [44] H Kuhn and A Tucker. Nonlinear programming. In *Proceedings of 2nd Berkeley symposium (pp. 481–492)*, 1951. [5](#)
- [45] Andrey Kurenkov, Jingwei Ji, Animesh Garg, Viraj Mehta, JunYoung Gwak, Christopher Choy, and Silvio Savarese. Deformnet: Free-form deformation network for 3d shape reconstruction from a single image. In *2018 IEEE Winter Conference on Applications of Computer Vision (WACV)*, pages 858–866. IEEE, 2018. [1](#)
- [46] Doyup Lee, Chiheon Kim, Saehoon Kim, Minsu Cho, and Wook-Shin Han. Autoregressive image generation using residual quantization. In *Proceedings of the IEEE/CVF Conference on Computer Vision and Pattern Recognition*, pages 11523–11532, 2022. [2](#), [3](#), [5](#)
- [47] Chun-Liang Li, Manzil Zaheer, Yang Zhang, Barnabas Poczos, and Ruslan Salakhutdinov. Point cloud gan. *arXiv preprint arXiv:1810.05795*, 2018. [2](#)
- [48] Ruihui Li, Xianzhi Li, Chi-Wing Fu, Daniel Cohen-Or, and Pheng-Ann Heng. Pu-gan: a point cloud upsampling adversarial network. In *Proceedings of the IEEE/CVF international conference on computer vision*, pages 7203–7212, 2019. [8](#), [17](#)
- [49] Shidi Li, Miaomiao Liu, and Christian Walder. Editvae: Unsupervised parts-aware controllable 3d point cloud shape generation. In *Proceedings of the AAAI Conference on Artificial Intelligence*, pages 1386–1394, 2022. [3](#)
- [50] Shidi Li, Christian Walder, and Miaomiao Liu. Spa-vae: Similar-parts-assignment for unsupervised 3d point cloud generation. *arXiv preprint arXiv:2203.07825*, 2022. [3](#)
- [51] Yushi Li and George Baciuc. Hsgan: Hierarchical graph learning for point cloud generation. *IEEE Transactions on Image Processing*, 30:4540–4554, 2021. [2](#)
- [52] Xinmiao Lin, Yikang Li, Jenhao Hsiao, Chiuman Ho, and Yu Kong. Catch missing details: Image reconstruction with frequency augmented variational autoencoder. In *Proceedings of the IEEE/CVF Conference on Computer Vision and Pattern Recognition*, pages 1736–1745, 2023. [3](#)
- [53] Songxiang Liu, Dan Su, and Dong Yu. Diffgan-tts: High-fidelity and efficient text-to-speech with denoising diffusion gans. *arXiv preprint arXiv:2201.11972*, 2022. [2](#)
- [54] Zhijian Liu, Haotian Tang, Yujun Lin, and Song Han. Point-voxel cnn for efficient 3d deep learning. *Advances in Neural Information Processing Systems*, 32, 2019. [2](#), [6](#)
- [55] David Lopez-Paz and Maxime Oquab. Revisiting classifier two-sample tests. *arXiv preprint arXiv:1610.06545*, 2016. [6](#), [15](#)
- [56] Shitong Luo and Wei Hu. Diffusion probabilistic models for 3d point cloud generation. In *Proceedings of the IEEE/CVF Conference on Computer Vision and Pattern Recognition*, pages 2837–2845, 2021. [1](#), [2](#), [3](#), [6](#), [7](#), [8](#), [16](#)
- [57] Ben Mildenhall, Pratul P Srinivasan, Matthew Tancik, Jonathan T Barron, Ravi Ramamoorthi, and Ren Ng. Nerf: Representing scenes as neural radiance fields for view synthesis. *Communications of the ACM*, 65(1):99–106, 2021. [2](#), [3](#)
- [58] Gautam Mittal, Jesse Engel, Curtis Hawthorne, and Ian Simon. Symbolic music generation with diffusion models. *arXiv preprint arXiv:2103.16091*, 2021. [2](#)

- [59] Shentong Mo, Enze Xie, Ruihang Chu, Lewei Yao, Lanqing Hong, Matthias Nießner, and Zhenguo Li. Dit-3d: Exploring plain diffusion transformers for 3d shape generation. *arXiv preprint arXiv:2307.01831*, 2023. 2
- [60] Aamir Mustafa, Param Hanji, and Rafal Mantiuk. Distilling style from image pairs for global forward and inverse tone mapping. In *Proceedings of the 19th ACM SIGGRAPH European Conference on Visual Media Production*, pages 1–10, 2022. 2
- [61] Hanieh Naderi, Kimia Noorbakhsh, Arian Etemadi, and Shohreh Kasaei. Lpf-defense: 3d adversarial defense based on frequency analysis. *Plos one*, 18(2):e0271388, 2023. 3
- [62] George Kiyohiro Nakayama, Mikaela Angelina Uy, Jiahui Huang, Shi-Min Hu, Ke Li, and Leonidas Guibas. Diff-facto: Controllable part-based 3d point cloud generation with cross diffusion. In *Proceedings of the IEEE/CVF International Conference on Computer Vision*, pages 14257–14267, 2023. 2
- [63] Kushagra Pandey, Avideep Mukherjee, Piyush Rai, and Abhishek Kumar. Diffusevae: Efficient, controllable and high-fidelity generation from low-dimensional latents. *arXiv preprint arXiv:2201.00308*, 2022. 2
- [64] Adam P Piotrowski and Jarosław J Napiorkowski. A comparison of methods to avoid overfitting in neural networks training in the case of catchment runoff modelling. *Journal of Hydrology*, 476:97–111, 2013. 2
- [65] Ben Poole, Ajay Jain, Jonathan T. Barron, and Ben Mildenhall. Dreamfusion: Text-to-3d using 2d diffusion. *arXiv*, 2022. 2
- [66] Konpat Preechakul, Nattanat Chatthee, Suttisak Widadwongsa, and Supasorn Suwajanakorn. Diffusion autoencoders: Toward a meaningful and decodable representation. In *Proceedings of the IEEE/CVF Conference on Computer Vision and Pattern Recognition*, pages 10619–10629, 2022. 2
- [67] Charles R Qi, Hao Su, Kaichun Mo, and Leonidas J Guibas. Pointnet: Deep learning on point sets for 3d classification and segmentation. In *Proceedings of the IEEE conference on computer vision and pattern recognition*, pages 652–660, 2017. 2, 6
- [68] Charles Ruizhongtai Qi, Li Yi, Hao Su, and Leonidas J Guibas. Pointnet++: Deep hierarchical feature learning on point sets in a metric space. *Advances in neural information processing systems*, 30, 2017. 2, 6
- [69] Guocheng Qian, Abdullellah Abualshour, Guohao Li, Ali Thabet, and Bernard Ghanem. Pu-gcn: Point cloud upsampling using graph convolutional networks. In *Proceedings of the IEEE/CVF Conference on Computer Vision and Pattern Recognition (CVPR)*, pages 11683–11692, 2021. 8, 17
- [70] Nasim Rahaman, Aristide Baratin, Devansh Arpit, Felix Draxler, Min Lin, Fred Hamprecht, Yoshua Bengio, and Aaron Courville. On the spectral bias of neural networks. In *International Conference on Machine Learning*, pages 5301–5310. PMLR, 2019. 3, 14
- [71] Ali Rahimi and Benjamin Recht. Random features for large-scale kernel machines. *Advances in neural information processing systems*, 20, 2007. 3
- [72] Aditya Ramesh, Prafulla Dhariwal, Alex Nichol, Casey Chu, and Mark Chen. Hierarchical text-conditional image generation with clip latents. *arXiv preprint arXiv:2204.06125*, 1(2):3, 2022. 2
- [73] Ali Razavi, Aaron Van den Oord, and Oriol Vinyals. Generating diverse high-fidelity images with vq-vae-2. *Advances in neural information processing systems*, 32, 2019. 6
- [74] Danilo Rezende and Shakir Mohamed. Variational inference with normalizing flows. In *International conference on machine learning*, pages 1530–1538. PMLR, 2015. 2, 6, 14
- [75] Danilo Jimenez Rezende, Shakir Mohamed, and Daan Wierstra. Stochastic backpropagation and approximate inference in deep generative models. In *International conference on machine learning*, pages 1278–1286. PMLR, 2014. 2
- [76] Robin Rombach, Andreas Blattmann, Dominik Lorenz, Patrick Esser, and Björn Ommer. High-resolution image synthesis with latent diffusion models. In *Proceedings of the IEEE/CVF Conference on Computer Vision and Pattern Recognition*, pages 10684–10695, 2022. 2, 5, 6
- [77] Olaf Ronneberger, Philipp Fischer, and Thomas Brox. U-net: Convolutional networks for biomedical image segmentation. In *Medical Image Computing and Computer-Assisted Intervention—MICCAI 2015: 18th International Conference, Munich, Germany, October 5–9, 2015, Proceedings, Part III 18*, pages 234–241. Springer, 2015. 6
- [78] Mihaela Rosca, Balaji Lakshminarayanan, and Shakir Mohamed. Distribution matching in variational inference. *arXiv preprint arXiv:1802.06847*, 2018. 2, 5
- [79] Andrés Serna, Beatriz Marcotegui, François Goulette, and Jean-Emmanuel Deschaud. Paris-rue-madame database: a 3d mobile laser scanner dataset for benchmarking urban detection, segmentation and classification methods. In *4th international conference on pattern recognition, applications and methods ICPRAM 2014*, 2014. 2
- [80] Dong Wook Shu, Sung Woo Park, and Junseok Kwon. 3d point cloud generative adversarial network based on tree structured graph convolutions. In *Proceedings of the IEEE/CVF international conference on computer vision*, pages 3859–3868, 2019. 2
- [81] Abhishek Sinha, Jiaming Song, Chenlin Meng, and Stefano Ermon. D2c: Diffusion-decoding models for few-shot conditional generation. *Advances in Neural Information Processing Systems*, 34:12533–12548, 2021. 2
- [82] Jascha Sohl-Dickstein, Eric Weiss, Niru Maheswaranathan, and Surya Ganguli. Deep unsupervised learning using nonequilibrium thermodynamics. In *International conference on machine learning*, pages 2256–2265. PMLR, 2015. 2, 3, 13
- [83] Yang Song, Liyue Shen, Lei Xing, and Stefano Ermon. Solving inverse problems in medical imaging with score-based generative models. *arXiv preprint arXiv:2111.08005*, 2021. 2
- [84] Yongbin Sun, Yue Wang, Ziwei Liu, Joshua Siegel, and Sanjay Sarma. Pointgrow: Autoregressively learned point cloud generation with self-attention. In *Proceedings of the*

- IEEE/CVF Winter Conference on Applications of Computer Vision*, pages 61–70, 2020. 3
- [85] Matthew Tancik, Pratul Srinivasan, Ben Mildenhall, Sara Fridovich-Keil, Nithin Raghavan, Utkarsh Singhal, Ravi Ramamoorthi, Jonathan Barron, and Ren Ng. Fourier features let networks learn high frequency functions in low dimensional domains. *Advances in Neural Information Processing Systems*, 33:7537–7547, 2020. 3
- [86] Jakub Tomczak and Max Welling. Vae with a vampprior. In *International Conference on Artificial Intelligence and Statistics*, pages 1214–1223. PMLR, 2018. 2, 5
- [87] Arash Vahdat, Karsten Kreis, and Jan Kautz. Score-based generative modeling in latent space. *Advances in Neural Information Processing Systems*, 34:11287–11302, 2021. 2, 5, 6
- [88] Arash Vahdat, Francis Williams, Zan Gojcic, Or Litany, Sanja Fidler, Karsten Kreis, et al. Lion: Latent point diffusion models for 3d shape generation. *Advances in Neural Information Processing Systems*, 35:10021–10039, 2022. 1, 2, 6, 7, 8, 16
- [89] Ashish Vaswani, Noam Shazeer, Niki Parmar, Jakob Uszkoreit, Llion Jones, Aidan N Gomez, Łukasz Kaiser, and Illia Polosukhin. Attention is all you need. *Advances in neural information processing systems*, 30, 2017. 3
- [90] Lei Wang, Yuchun Huang, Pengjie Tao, Yaolin Hou, and Yuxuan Liu. Learning geometry-image representation for 3d point cloud generation. *arXiv preprint arXiv:2011.14289*, 2020. 3
- [91] Yuehui Wang, Liyan Cai, Dongyu Zhang, and Sibohuang. The frequency discrepancy between real and generated images. *IEEE Access*, 9:115205–115216, 2021. 3
- [92] Jay Whang, Erik Lindgren, and Alex Dimakis. Composing normalizing flows for inverse problems. In *International Conference on Machine Learning*, pages 11158–11169. PMLR, 2021. 2
- [93] Lemeng Wu, Dilin Wang, Chengyue Gong, Xingchao Liu, Yunyang Xiong, Rakesh Ranjan, Raghuraman Krishnamoorthi, Vikas Chandra, and Qiang Liu. Fast point cloud generation with straight flows. In *Proceedings of the IEEE/CVF Conference on Computer Vision and Pattern Recognition*, pages 9445–9454, 2023. 1, 2
- [94] Zhi-Qin John Xu, Yaoyu Zhang, Tao Luo, Yanyang Xiao, and Zheng Ma. Frequency principle: Fourier analysis sheds light on deep neural networks. *arXiv preprint arXiv:1901.06523*, 2019. 3
- [95] Guandao Yang, Xun Huang, Zekun Hao, Ming-Yu Liu, Serge Belongie, and Bharath Hariharan. Pointflow: 3d point cloud generation with continuous normalizing flows. In *Proceedings of the IEEE/CVF international conference on computer vision*, pages 4541–4550, 2019. 2, 3, 4, 6, 7, 8, 15, 16
- [96] Yaoqing Yang, Chen Feng, Yiru Shen, and Dong Tian. Foldingnet: Point cloud auto-encoder via deep grid deformation. In *Proceedings of the IEEE conference on computer vision and pattern recognition*, pages 206–215, 2018. 1, 2, 3
- [97] Lequan Yu, Xianzhi Li, Chi-Wing Fu, Daniel Cohen-Or, and Pheng-Ann Heng. Ec-net: an edge-aware point set consolidation network. In *Proceedings of the European conference on computer vision (ECCV)*, pages 386–402, 2018. 1
- [98] Maciej Zamorski, Maciej Zięba, Piotr Klukowski, Rafał Nowak, Karol Kurach, Wojciech Stokowiec, and Tomasz Trzcíński. Adversarial autoencoders for compact representations of 3d point clouds. *Computer Vision and Image Understanding*, 193:102921, 2020. 1, 2
- [99] Ruonan Zhang, Jingyi Chen, Wei Gao, Ge Li, and Thomas H Li. Pointot: Interpretable geometry-inspired point cloud generative model via optimal transport. *IEEE Transactions on Circuits and Systems for Video Technology*, 32(10):6792–6806, 2022. 2
- [100] Yu Zhang, Peter Tiño, Aleš Leonardis, and Ke Tang. A survey on neural network interpretability. *IEEE Transactions on Emerging Topics in Computational Intelligence*, 5(5):726–742, 2021. 2
- [101] Daquan Zhou, Weimin Wang, Hanshu Yan, Weiwei Lv, Yizhe Zhu, and Jiashi Feng. Magicvideo: Efficient video generation with latent diffusion models. *arXiv preprint arXiv:2211.11018*, 2022. 2
- [102] Linqi Zhou, Yilun Du, and Jiajun Wu. 3d shape generation and completion through point-voxel diffusion. In *Proceedings of the IEEE/CVF International Conference on Computer Vision*, pages 5826–5835, 2021. 1, 2, 6, 7, 8, 16

FrePolad: Frequency-Rectified Point Latent Diffusion for Point Cloud Generation

Supplementary Material

A. Denoising Diffusion Probabilistic Model

Given a data sample $\mathbf{z} \sim q(\mathbf{z})$, at each time step $t = 1, 2, \dots, T$, DDPMs [29, 82] gradually transform $\mathbf{z} = \mathbf{z}_0$ into \mathbf{z}_T by adding noise in a Markovian *diffusion process* defined by

$$q(\mathbf{z}_{1:T}|\mathbf{z}_0) := \prod_{t=1}^T q(\mathbf{z}_t|\mathbf{z}_{t-1}); \quad (18)$$

$$q(\mathbf{z}_t|\mathbf{z}_{t-1}) := \mathcal{N}\left(\sqrt{1-\beta_t}\mathbf{z}_{t-1}, \beta_t I\right), \quad (19)$$

where $\mathcal{N}(\boldsymbol{\mu}, \boldsymbol{\sigma})$ denotes multivariate Gaussian distribution with mean $\boldsymbol{\mu}$ and variance $\boldsymbol{\sigma}$, and $\{\beta_t\}_t$ is a pre-determined variance schedule controlling the rate of diffusion. If T is sufficiently large (1000 steps in practice), $p(\mathbf{z}_T)$ approaches the standard Gaussian.

DDPMs learn an inverse Markovian process called *reverse process* parametrized by ζ that inverts the forward diffusion, transforming the standard Gaussian noise \mathbf{z}_T back to a data sample:

$$p_\zeta(\mathbf{z}_{0:T}) := p(\mathbf{z}_T) \prod_{t=1}^T p_\zeta(\mathbf{z}_{t-1}|\mathbf{z}_t); \quad (20)$$

$$p_\zeta(\mathbf{z}_{t-1}|\mathbf{z}_t) := \mathcal{N}\left(\mu_\zeta(\mathbf{z}_t, t), \sigma_t^2 I\right), \quad (21)$$

where $\mu_\zeta(\mathbf{z}_t, t)$ represents the predicted mean for the Gaussian distribution at time step t and $\{\sigma_t\}_t$ is the variance schedule.

DDPMs are trained by maximizing the variational lower bound of log-likelihood of the data \mathbf{z}_0 under $q(\mathbf{z}_0)$:

$$\mathbb{E}_{q(\mathbf{z}_0)} [\log p_\zeta(\mathbf{z}_0)] \geq \mathbb{E}_{q(\mathbf{z}_{0:T})} \left[\log \frac{p_\zeta(\mathbf{z}_{0:T})}{q(\mathbf{z}_{1:T}|\mathbf{z}_0)} \right]. \quad (22)$$

Expanding Eq. (22) with Eq. (20) and noticing that $p(\mathbf{z}_T)$ and $q(\mathbf{z}_{1:T}|\mathbf{z}_0)$ are constant with respect to ζ , we obtain our objective function to maximize:

$$\mathbb{E}_{q(\mathbf{z}_0), q(\mathbf{z}_{1:T}|\mathbf{z}_0)} \left[\sum_{t=1}^T \log p_\zeta(\mathbf{z}_{t-1}|\mathbf{z}_t) \right]. \quad (23)$$

Since we can factor the joint posterior

$$q(\mathbf{z}_{1:T}|\mathbf{z}_0) = \prod_{t=1}^T q(\mathbf{z}_{t-1}|\mathbf{z}_t, \mathbf{z}_0) \quad (24)$$

and both $q(\mathbf{z}_{t-1}|\mathbf{z}_t, \mathbf{z}_0)$ and $p_\zeta(\mathbf{z}_{t-1}|\mathbf{z}_t)$ are Gaussian, maximizing Eq. (23) can be reduced to minimizing the following loss:

$$\mathcal{L}_{\text{DDPM}}(\zeta) := \mathbb{E}_{q(\mathbf{z}_0), t \sim \mathcal{U}(1, T), \epsilon \sim \mathcal{N}(0, I)} [\|\epsilon - \epsilon_\zeta(\mathbf{z}_t, t)\|_2^2], \quad (25)$$

where $\mathcal{U}(1, T)$ is the uniform distribution on $\{1, 2, \dots, T\}$. Note that here we employ a commonly used parametrization

$$\mu_\zeta(\mathbf{z}_t, t) = \frac{1}{\sqrt{1-\beta_t}} \left(\mathbf{z}_t - \frac{\beta_t}{\gamma_t} \epsilon_\zeta(\mathbf{z}_t, t) \right) \quad (26)$$

and that via Eq. (19) \mathbf{z}_t is in fact tractable from the initial \mathbf{z}_0 by

$$\mathbf{z}_t = \alpha_t \mathbf{z}_0 + \gamma_t \epsilon, \quad (27)$$

where $\alpha_t := \prod_{i=1}^t \sqrt{1-\beta_i}$ and $\gamma_t := \sqrt{1-\alpha_t^2}$. Intuitively, minimizing the loss Eq. (25) amounts to predict the noise ϵ necessary to denoise the diffused sample \mathbf{z}_t .

During inference time, DDPMs can be iteratively sampled with ancestral sampling by first sampling \mathbf{z}_T from $p(\mathbf{z}_T) := \mathcal{N}(0, I)$ and following Eq. (21); that is:

$$p_\zeta(\mathbf{z}) = p(\mathbf{z}_T) p_\zeta(\mathbf{z}|\mathbf{z}_T) = p(\mathbf{z}_T) \prod_{t=1}^T p_\zeta(\mathbf{z}_{t-1}|\mathbf{z}_t) \quad (28)$$

for $p(\mathbf{z}_T) := \mathcal{N}(0, I)$.

B. Spherical Harmonics

The spherical harmonics [10] are a set of complex-valued spherical harmonic base functions $Y_{l,m} : S^2 \rightarrow \mathbb{C}$ defined on a unit sphere S^2 , indexed by the degree $l \geq 0$ and order m ($-l \leq m \leq l$):

$$Y_{l,m}(\theta, \varphi) := Z_{l,m} e^{im\varphi} P_{l,m}(\cos \theta), \quad (29)$$

where the colatitud $\theta \in [0, \pi]$, the longitude $\varphi \in [0, 2\pi]$, $Z_{l,m} \in \mathbb{C}$ is the normalization constant, i is the imaginary unit, and $P_{l,m} : [-1, 1] \rightarrow \mathbb{R}$ is the associated Legendre polynomial of degree l and order m satisfying the general Legendre equation:

$$\frac{d}{dx} \left[(1-x^2) \frac{d}{dx} P_{l,m}(x) \right] + \left[l(l+1) - \frac{m^2}{1-x^2} \right] P_{l,m}(x) = 0. \quad (30)$$

Note that for a fixed degree l , any $Y_{l,m}$ for $-l \leq m \leq l$ are solutions to the differential equation

$$\Delta Y_{l,m} = -l(l+1)Y_{l,m}, \quad (31)$$

where Δ is the Laplace operator, and that every solution to Eq. (31) is a linear combination of $Y_{l,m}$, $-l \leq m \leq l$. In other words, spherical harmonics base functions are eigenfunctions of the Laplace operator (or, more generally in higher dimensions, the Laplace-Beltrami operator).

The spherical harmonics are a complete set of orthonormal functions and thus form an orthonormal basis for square-intergrable functions defined on the unit sphere $L^2(S^2)$ [70]; *i.e.*, every continuous function $f : S^2 \rightarrow \mathbb{C}$ such that

$$\int_0^{2\pi} \int_0^\pi |f(\theta, \varphi)|^2 d\theta d\varphi < \infty \quad (32)$$

can be represented as a series of these spherical harmonic base functions $Y_{l,m}$ by

$$f(\theta, \varphi) = \sum_{l=0}^{\infty} \sum_{m=-l}^l c_{l,m} Y_{l,m}(\theta, \varphi), \quad (33)$$

where the coefficients $c_{l,m}$ can be calculated by

$$c_{l,m} = \int_0^{2\pi} \int_0^\pi f(\theta, \varphi) \overline{Y_{l,m}(\theta, \varphi)} \sin(\theta) d\theta d\varphi. \quad (34)$$

This is parallel to the result from Fourier analysis [20] that any arbitrary function defined on a plane can be expressed as a trigonometric series. The trigonometric functions in a Fourier series capture the fundamental modes of vibration on a plane whereas the spherical harmonics denote these modes of vibration on a sphere. Consequently, spherical harmonics cast spatial data into the spectral domain, allowing the extraction of frequency-specific information: coefficients $c_{l,m}$ with a higher degree measure the intensity of the original data in a higher-frequency domain. Please refer to Sec. B in the supplementary for more details about spherical harmonics.

C. Continuous Normalizing Flow

Normalizing flows [74] consist of a sequence of reversible mappings $\{g^i\}_{i=1}^n$. It assumes that the data points $\mathbf{x} = \mathbf{x}_n$ are obtained by iteratively transforming a sample from an initial distribution $p(\mathbf{x}_0)$:

$$\mathbf{x}_n := (g^n \circ g^{n-1} \circ \dots \circ g^1)(\mathbf{x}_0). \quad (35)$$

The probability density of the resultant variable \mathbf{x}_n can be determined using the change of variables formula:

$$\log p(\mathbf{x}_n) = \log p(\mathbf{x}_0) - \sum_{i=1}^n \log \left| \det \left(\frac{\partial g^i(\mathbf{x}_{i-1})}{\partial \mathbf{x}_{i-1}} \right) \right|, \quad (36)$$

where \mathbf{x}_0 can be computed from \mathbf{x}_n using the inverse flow

$$\mathbf{x}_0 = (g^1 \circ \dots \circ g^{n-1} \circ g^n)(\mathbf{x}_n), \quad (37)$$

and $\det(\cdot)$ is the Jacobian determinant function.

In practice, the initial distribution $p(\mathbf{x}_0)$ is chosen to be the standard Gaussian $\mathcal{N}(0, I)$, and the invertible mappings $\{g^i\}_{i=1}^n$ are represented by neural networks $\{g_\xi^i\}_{i=1}^n$ parameterized by ξ for which the Jacobian determinant $\left| \det \left(\frac{\partial g_\xi^i(\mathbf{x}_{i-1})}{\partial \mathbf{x}_{i-1}} \right) \right|$ is easy to compute. Since the exact log-likelihood of input data is tractable via Eq. (36), the training of normalizing flows just involves maximizing Eq. (36).

Normalizing flows can be generalized to continuous normalizing flows (CNFs) [8, 25], where a sequence of mappings $\{g_\xi(\cdot, t)\}_{t=0}^\tau$ indexed by a real number $t \in \mathbb{R}$ transforms an initial point $\mathbf{x}(0) \sim p(\mathbf{x}_0)$ into $\mathbf{x}(\tau)$ following a continuous-time dynamic

$$\frac{\partial \mathbf{x}_t}{\partial t} = g_\xi(\mathbf{x}(t), t), \quad (38)$$

and therefore

$$\mathbf{x}(\tau) = \mathbf{x}(0) + \int_0^\tau g_\xi(\mathbf{x}(0), t) dt. \quad (39)$$

Under this formulation, the probability density function $p(\mathbf{x}(\tau))$ of the transformed variable $\mathbf{x}(\tau)$ can be determined via

$$\log p(\mathbf{x}(\tau)) = \log p(\mathbf{x}(0)) - \int_0^\tau \text{Tr} \left(\frac{\partial g_\xi(\mathbf{x}(t), t)}{\partial \mathbf{x}(t)} \right), \quad (40)$$

where $\mathbf{x}(0)$ can be computed from $\mathbf{x}(\tau)$ by

$$\mathbf{x}(0) = \mathbf{x}(\tau) - \int_0^\tau g_\xi(\mathbf{x}(0), t) dt, \quad (41)$$

and $\text{Tr}(\cdot)$ is the trace function. Similarly, the training of CNFs amounts to maximizing the data log-likelihood Eq. (40).

CNFs can be further extended to be conditioned on a vector \mathbf{z} by using $g_\xi(\cdot, t, \mathbf{z})$ in place of $g_\xi(\cdot, t)$. This allows to compute the conditional probability of the data conditioned on \mathbf{z} :

$$\log p(\mathbf{x}(\tau)|\mathbf{z}) = \log p(\mathbf{x}(0)) - \int_0^\tau \text{Tr} \left(\frac{\partial g_\xi(\mathbf{x}(t), t, \mathbf{z})}{\partial \mathbf{x}(t)} \right); \quad (42)$$

$$\mathbf{x}(0) = \mathbf{x}(\tau) - \int_0^\tau g_\xi(\mathbf{x}(0), t, \mathbf{z}) dt. \quad (43)$$

To sample a CNF, we first sample an initial point $\mathbf{x}(0) \sim p(\mathbf{x}_0)$, then simply follow Eq. (39).

D. Training Details

In all experiments we set $D_z = 1024$, $k = 5$ in Eq. (8), $\sigma_{\text{KNN}} = 0.05$ in Eq. (9), $\eta = 5 \times 10^6$ in Eq. (15), and $L = 50$ and $\sigma_{\text{Fre}} = 50$ in Eq. (11).

We use an Adam optimizer with an initial learning rate of 10^{-3} for VAE training and 10^{-5} for latent DDPM training with $\beta_1 = 0.9$ and $\beta_2 = 0.999$. We use a weight decay of 10^{-8} . During training, the learning rate is decayed by a factor of 10 whenever the loss plateaus for more than five epochs.

We run all experiments on a machine with a single GPU Nvidia GeForce RTX 4090. Where relevant, all DDPMs are sampled using 1000 time steps.

E. Further Quantitative Comparisons

We present further quantitative comparisons of different models on point cloud generation task by considering more metrics and more ShapeNet data classes. We employ three evaluative scores for generative models: minimum matching distance (MMD) [1], coverage (COV) [1], and 1-nearest neighbor (1-NNA) [55]. Each score can be computed using Chamfer distance (CD) or earth mover distance (EMD), totaling six metrics. While MMD gauges generation fidelity, it remains insensitive to suboptimal samples. Conversely, COV quantifies generation diversity, and 1-NNA measures the distributional similarity between two sets of point clouds, taking both diversity and quality into account. More detailed discussion regarding these metrics can be found in [95].

Table 5 is the full version of Tab. 1 for quantitative comparison of point cloud generation task on three classes of ShapeNet dataset. Table 6 is the full version of Tab. 2 for FrePolad’s ablation study. Table 7 is the full version of Tab. 4 comparing the performance of FrePolad’s direct generation of dense point clouds against generation via upsampling from sparse point clouds using various upsampling methods.

Class	Model	MMD ↓		COV (%) ↑		1-NNA (%) ↓	
		CD	EMD	CD	EMD	CD	EMD
Airplane	Training set	0.218	0.373	46.91	52.10	64.44	64.07
	r-GAN [1]	0.447	2.309	30.12	14.32	98.40	96.79
	1-GAN (CD) [1]	0.340	0.583	38.52	21.23	87.30	93.95
	1-GAN (EMD) [1]	0.397	0.417	38.27	38.52	89.49	76.91
	PointFlow [95]	0.224	0.390	47.90	46.41	75.68	70.74
	SoftFlow [36]	0.231	0.375	46.91	47.90	76.05	65.80
	SetVAE [37]	0.200	0.367	43.70	48.40	76.54	67.65
	ShapeGF [4]	0.313	0.637	45.19	40.25	81.23	80.86
	DPF-Net [43]	0.264	0.409	46.17	48.89	75.18	65.55
	DPC [56]	0.213	0.572	48.64	33.83	76.42	86.91
	PVD [102]	0.224	0.370	48.88	52.09	73.82	64.81
	LION [88]	0.219	0.372	47.16	49.63	67.41	61.23
	FrePolad (ours)	0.204	0.353	45.16	47.80	65.25	62.10
	Chair	Training set	2.618	1.555	53.02	51.21	51.28
r-GAN [1]		5.151	8.312	24.27	15.13	83.69	99.70
1-GAN (CD) [1]		2.589	2.007	41.99	29.31	68.58	83.84
1-GAN (EMD) [1]		2.811	1.619	38.07	44.86	71.90	64.65
PointFlow [95]		2.409	1.595	42.90	50.00	62.84	60.57
SoftFlow [36]		2.528	1.682	41.39	47.43	59.21	60.05
SetVAE [37]		2.545	1.585	46.83	44.26	58.84	60.57
ShapeGF [4]		3.724	2.394	48.34	44.26	58.01	61.25
DPF-Net [43]		2.536	1.632	44.71	48.79	62.00	58.53
DPC [56]		2.399	2.066	44.86	35.50	60.05	74.77
PVD [102]		2.622	1.556	49.84	50.60	56.26	53.32
LION [88]		2.640	1.550	48.94	52.11	53.70	52.34
FrePolad (ours)		2.542	1.532	50.28	50.93	52.35	53.23
Car		Training set	0.938	0.791	50.85	55.68	51.70
	r-GAN [1]	1.446	2.133	19.03	6.539	94.46	99.01
	1-GAN (CD) [1]	1.532	1.226	38.92	23.58	66.49	88.78
	1-GAN (EMD) [1]	1.408	0.899	37.78	45.17	71.16	66.19
	PointFlow [95]	0.901	0.807	46.88	50.00	58.10	56.25
	SoftFlow [36]	1.187	0.859	42.90	44.60	64.77	60.09
	SetVAE [37]	0.882	0.733	49.15	46.59	59.94	59.94
	ShapeGF [4]	1.020	0.824	44.03	47.19	61.79	57.24
	DPF-Net [43]	1.129	0.853	45.74	49.43	62.35	54.48
	DPC [56]	0.902	1.140	44.03	34.94	68.89	79.97
	PVD [102]	1.007	0.794	41.19	50.56	54.55	53.83
	LION [88]	0.913	0.752	50.00	56.53	53.41	51.14
	FrePolad (ours)	0.904	0.782	50.14	55.23	51.89	50.26

Table 5. Quantitative comparison of point cloud generation on three classes of ShapeNet dataset. MMD-CD is multiplied by 10^3 and MMD-EMD is multiplied by 10^2 . FrePolad achieves significant improvement over most existing models and obtains state-of-the-art results with simpler and more flexible structure.

Class	Model	MMD ↓		COV (%) ↑		1-NNA (%) ↓	
		CD	EMD	CD	EMD	CD	EMD
Airplane	Training set	0.218	0.373	46.91	52.10	64.44	64.07
	Po	0.871	0.804	23.44	35.06	85.93	85.94
	FrePo	0.757	0.730	26.56	40.38	80.38	80.38
	Polad	0.279	0.383	45.12	47.96	69.26	65.26
	FrePolad	0.204	0.353	45.16	47.80	65.25	62.10
Chair	Training set	2.618	1.555	53.02	51.21	51.28	54.76
	Po	5.253	3.393	17.19	14.06	94.53	99.22
	FrePo	5.160	2.498	24.06	27.19	89.06	82.19
	Polad	2.721	1.642	48.23	47.73	57.35	61.52
	FrePolad	2.542	1.532	50.28	50.93	52.35	53.23
Car	Training set	0.938	0.791	50.85	55.68	51.70	50.00
	Po	1.866	11.24	18.75	9.375	100.0	100.0
	FrePo	1.011	2.057	27.81	28.75	89.22	84.53
	Polad	1.148	0.817	46.23	49.10	58.12	56.13
	FrePolad	0.904	0.782	50.14	55.23	51.89	50.26

Table 6. Ablation study: quantitative comparison of three weakened versions of FrePolad: Polad (without frequency rectification), FrePo (without latent diffusion), and Po (without either). MMD-CD is multiplied by 10^3 and MMD-EMD is multiplied by 10^2 . The frequency rectification and the latent DDPM bring significant improvement to FrePolad.

Class	Model	8192		15k		100k	
		CD	EMD	CD	EMD	CD	EMD
Airplane	PU-GAN [48]	100	99.38	100	99.06	100	99.06
	PU-GCN [69]	100	99.38	100	99.38	100	99.38
	Grad-PU [28]	100	99.38	100	99.38	100	99.38
	FrePolad (ours)	65.31	63.88	66.87	57.81	66.25	60.25
Chair	PU-GAN [48]	100	100	100	100	100	100
	PU-GCN [69]	100	100	100	100	100	100
	Grad-PU [28]	100	100	100	100	100	100
	FrePolad (ours)	52.69	50.63	53.63	50.00	52.69	51.56
Car	PU-GAN [48]	99.06	98.75	99.06	98.75	99.06	98.13
	PU-GCN [69]	99.38	99.06	99.38	99.06	99.38	99.06
	Grad-PU [28]	99.38	98.75	99.38	98.75	99.38	98.75
	FrePolad (ours)	52.06	54.25	52.06	51.75	51.13	51.50

Table 7. 1-NNA scores (\downarrow) of the generated dense point clouds with different cardinalities. FrePolad directly generates dense point clouds. The first three methods upsample sparse ground truth ones. FrePolad profoundly outperforms all upsampling methods, demonstrating the importance of the ability to directly generate dense point clouds.